UAV-BASED URBAN MONITORING USING ON-BOARD 802.11AD RADAR

Shobha Sundar Ram[†] *and Kumar Vijay Mishra*[‡]

[†]Indraprastha Institute of Information Technology Delhi, New Delhi 110020 India
[‡]United States DEVCOM Army Research Laboratory, Adelphi, MD 20783 USA

2022 IEEE 12th Sensor Array and Multichannel Signal Processing Workshop (SAM) | 978-1-6654-0633-8/22/$31.00 ©2022 IEEE | DOI: 10.1109/SAM53842.2022.9827834

ABSTRACT

The unmanned aerial vehicles (UAVs) offer low-cost, flexible, and line-of-sight deployment for radar remote sensing as well as building temporary communications base stations in inaccessible or crowded areas. Their limited battery power and small footprints is driving innovations to combine multiple functions in single hardware operating in the same spectrum. In particular, UAV-borne joint radar-communications (JRC) systems are of significant interest. In this paper, we focus on a wide-bandwidth millimeter-wave JRC system for UAVs that employ IEEE 802.11ad protocol for sensing. We model such a system for detecting dynamic users on the ground such as pedestrians and vehicles. Our method incorporates a realistic electromagnetic scattering center model of road targets and surface clutter in the pyBullet software to examine 802.11ad for UAV-borne sensing. Numerical experiments demonstrate that 802.11ad UAV-borne sensing is able to capture several micro-Doppler characteristics.

***Index Terms*—** Beam positioning, IEEE 802.11ad, joint radar-communications, micro-Doppler, UAV base station.

1. INTRODUCTION

Recently, aerial base stations (BSs) that are mounted on high-altitude pseudo-satellites (HAPS) such as airships, balloons, or unmanned aerial vehicles (UAVs) are increasingly investigated to augment the performance of fifth- or sixth-generation (5/6G) wireless networks [1–3]. The rapid deployment, adaptable relocation, and higher accessibility to light-of-sight (LOS) propagation links make these platforms very useful for scenarios such as congested urban environments [4], natural disasters, and blockage from mountains or forests [5, 6]. In particular, the wireless communication links on HAPS/UAV platforms have short endurance because of limited battery power [7]. This is often overcome through design of efficient flight routes [8], low-power hardware [9], and joint operation of a swarm of multiple drones [10, 11].

In HAPS-based aerial platforms, limited battery power and minimal hardware implies judicious use of available resources [12, 13]. In general, radars and wireless communications are essential sensors on modern UAVs to achieve active sensing to find occluded targets-of-interest as well as to function as temporary communications infrastructure at unreachable sites [14]. For UAVs that employ multiple sensors, it has been suggested to combine multiple functionalities on a single hardware to save power, area, spectrum, and cost [15]. Hence, development of transceivers that integrate radar and communications functions in the same UAV using a common radio spectrum is of immense interest [16]. Lately, millimeter-wave (mmWave) band has been suggested for aerial BS because not only it offers small form factor for the airborne hardware but also very wide bandwidth to support high data rates and radar range resolution [16, 17]. Such mmWave UAV-borne systems (Fig. 1) are envisaged to connect to dynamic users on the ground such as pedestrians and vehicles [18].

The JRC systems may employ customized or existing signaling methods for both sensing and communications [16, 19–21]. In particular, the use of an existing communications protocol for sensing functionality is very attractive because it makes use of available hardware and avoids redesign or developing a new system altogether. In this context, the IEEE 802.11ad protocol based on 60 GHz carrier frequency has been identified as one of the potential candidates for inter vehicular communication links [22]. Instead of omnidirectional beam patterns, IEEE 802.11ad facilitates digital beamforming and steers narrow beams to the users in order to obtain high quality-of-service in both active [23] and passive [24] systems. The direction of the road users may be estimated through channel estimation capabilities within the protocol. However, these capabilities usually result in a large overhead. The alternative solution is to augment the communication platform with auxiliary sensors such as radars for estimating the location of the users to facilitate beam alignment [25–27].

The IEEE 802.11ad-based JRC was first investigated in [22, 28]. Here, Golay complementary sequences [29, 30] within the channel estimation field of the preamble of the protocol were exploited for range estimation of point targets at long ranges. In [18], an ultra short-range 802-11ad-based JRC was proposed for tracking automotive targets using Golay sequences that were Doppler-resilient [31]. Radar imaging of automotive targets from a stationary BS was explored recently in [32].

In this paper, we propose an IEEE 802.11ad based JRC mounted on a UAV for tracking and communication with vehicles and pedestrians on the ground. In general, a drone-borne radar suffers from perturbations in hovering motion and undesired reflections (clutter) from buildings, terrain, and vegetation. We utilize extended scattering center models to simulate realistic aerial radar target signatures. Our numerical experiments incorporate complex target motions and UAV-ground propagation modeled as two-ray and surface-based clutter. This work is a promising precursor to beamforming using a swarm of 802.11ad-based HRC drones. Further, the swarm operation guarantees that sensing information is not completely lost when one of the drones has to shut down because of low battery [33].

2. UAV-BORNE 802.11AD-BASED JRC

A UAV hovers at low altitude of 50m above a flat ground. Therefore, we assume that the radar platform is stationary. Consider a drone equipped with a single antenna that transmits 802.11ad packets toward the targets-of-interest. The range and Doppler estimation methods using the single-carrier physical layer (SCPHY) channel

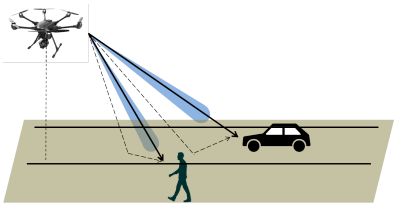

Fig. 1. Joint radar-communication platform mounted on drone to enable sensing of dynamic targets on ground.

estimation field (CEF) of standard 802.11ad are detailed in [27, 28, 30]. We recall the procedure briefly below.

2.1. Signal Model

The SCPHY CEF of 802.11ad encapsulates unimodular *Golay complementary pair* sequences $G_{1,N}$ and $G_{2,N}$ of the same length $N = 256$. There are two such distinct pairs present in the CEF; in other words, there are four individual sequences of length 256. These sequences have the property that the sum of their autocorrelations has a peak of $2N$ and a side-lobe level of zero, i.e.

$$G_{1,N}[n] * G_{1,N}[-n] + G_{2,N}[n] * G_{2,N}[-n] = 2N\delta[n]. \quad (1)$$

In particular, for the pth packet, the transmit signal is the 512-bit Golay sequence $s_T[n] = G_{p,512}[n]$, $n = 0, 1, \cdots, 511$, where $G_{p,512}$ and $G_{p+1,512}$ are Golay complementary pairs. The discrete-time sequence $s_T[n]$ is passed through a digital-to-analog-converter (DAC) the output of which can be represented as a weighted sum of Dirac impulses, $s_T(t) = \sum_{n=0}^{511} s_T[n]\delta(t - nT_c)$, where $F_c = 1.76$ GHz $= 1/T_c$. The resulting continuous-time signal is $x_T(t) = \sqrt{E_s}(s_T * h_T)(t) = \sum_{n=0}^{511} s_T[n]h_T(t - nT_c)$, where $h_T(t)$ represents the transmit shaping (Nyquist) filter.

Assume that the radar transmits P packets constituting one coherent processing interval (CPI) towards a direct-path extended target of B point scatterers, wherein each b^{th} point scatterer has the following unknown attributes: time-varying complex reflectivity a_b; range $r_b = c\tau_b/2$ relative to the UAV's location, where $c = 3 \times 10^8$ m/s is the speed of light and τ_b is the time delay; and Doppler frequency $f_{D_b} = \frac{2v_b}{\lambda}$ that is linearly proportional to the radial velocity v_b, where λ is the operating wavelength of the radar. T backscattered received signal at the baseband over a duration of a CPI is

$$\begin{aligned} & x_R(t) \\ &= \sum_{p=0}^{P-1}\sum_{b=1}^{B} a_b(t)x_T(t - \tau_b - pT_p)e^{-j2\pi f_{D_b}t} + c(t) + z(t) \\ &\approx \sum_{p=0}^{P-1}\sum_{b=1}^{B} a_b(t)x_T(t - \tau_b - pT_p)e^{-j2\pi f_{D_b}pT_p} \\ &\qquad + c(t) + z(t), \end{aligned} \quad (2)$$

where $c(t)$ represents the ground clutter, $z(t)$ is additive circular-symmetric white Gaussian noise, and the last approximation follows from the fact the phase rotation within one CPI (*slow time*) can be approximated as a constant, i.e. $f_{D_b} \ll 1/T_p$. Sampling the signal at $F_c = 1/T_c$ and Nyquist filter properties [18, 27], we obtain $x_R[n] = x_R(nT_c)$:

$$\begin{aligned} x_R[n] &= \sum_{p=0}^{P-1}\sum_{b=1}^{B} a_b[n]s_T(nT_c - \tau_b - pT_p)e^{-j2\pi f_{D_b}pT_p} \\ &\quad + c[n] + z[n]. \end{aligned} \quad (3)$$

A large body of literature exists on clutter removal algorithms in radars [34–37]. In classical radar signal processing, moving target indication (MTI) and moving target detection (MTD) exploit the difference in Doppler velocities of target and clutter to suppress clutter in frequency domain [38]. When the clutter statistics are known, the combined contribution from clutter and noise is first whitened and then processed through a matched-filter in digital domain [39]. In some specialized systems, this step is replaced by a *mismatched filter* with a different optimization metric such as minimization of peak-to-sidelobe-ratio of the output [40, 41]. After clutter removal, the sampled signal from two consecutive packets is passed through matched filters of each Golay sequence. Correlation the p^{th} pair produces $\hat{h}_p[n] = x_R[n] * G_{p,512}[-n]$ and $\hat{h}_{p+1}[n] = x_R[n] * G_{p+1,512}[-n]$. These outputs are added to return the channel estimate

$$\begin{aligned} \hat{h}[n] &= \frac{1}{1024}(\hat{h}_p[n] + \hat{h}_{p+1}[n]) \\ &\approx \frac{1}{1024}\sum_{p=0}^{P-1}\sum_{b=1}^{B} a_b[n]\delta(nT_c - \tau_b - pT_p)e^{-j2\pi f_{D_b}pT_p} \\ &\quad + z[n] * (G_{p,512}[-n] + G_{p+1,512}[-n]), \end{aligned} \quad (4)$$

where the last approximation is due to the assumption that the Doppler shifts are nearly identical for the two Golay sequences $G_{p,512}$ and $G_{p+1,512}$. The final channel estimate is the average over both Golay pairs.

We discretize the range-time space in, say, N bins of resolution $cT_c/2$. Take a P-point Discrete Fourier Transform (DFT) of the radar channel estimates corresponding to each delay bin to generate a delay-Doppler plane. Then the first B peaks in this plane yield the location of the delay and radial (Doppler) frequencies of the targets.

3. DYNAMIC UAV ROAD TARGET MODELS

The received data over each CPI from a target can be regarded as a two-dimensional matrix with $p = 1 : P$ frames constituting the slow time dimension; and $n = 1 : N$ bits in the CEF within each frame forming the fast time dimension. This data matrix is processed with Fourier processing across the slow time axis and matched filtering across the fast time axis to generate two-dimensional range-Doppler ambiguity plots, $\chi(r, f_d)$, for each CPI. In real world scenarios, the target may be regarded as an extended target with multiple scattering centers. Also, the radar returns usually consists of reflections from We discuss the models for the radar propagation, speckle noise and surface clutter in the following sections.

3.1. UAV-to-ground channel

Recently, there have been several different detailed studies of propagation links between aerial transmitters and ground based receivers [42]. In [43], systematic measurements of UAV-ground channels were carried out. Other works have discussed the modeling of UAV-ground channels. The UAV-ground links are LOS in most scenarios with occasional blockages due to terrain features such as buildings and vegetation. Besides the direct-path, the propagation is characterized by multipath components from surfaces, diffraction around the edges of sharp obstacles and clutter from ground and vegetation. Stochastic frameworks such as the Rician fading model have been

used to simulate the deterministic strong LOS component and the randomly scattered clutter components [44].

In this work, we have used a two-ray framework to simulate the effect of the direct wave and the surface reflected components. This model was earlier adopted in [45] to simulate propagation over flat terrains. Due to the short propagation distance, we ignore the earth's curvature. Instead, we have considered the earth to be a planar dielectric surface with a uniform lossy dielectric constant $(\epsilon_r' - j\epsilon_r'')$. Based on field equivalence principles, we model the ground effect by considering images of each of the point scatterers to be located at $\vec{r}_{b'}[n] = (x_b[n], y_b[n], -z_b[n]), b = 1 : B$. Then the one-way propagation factor between the radar and each point scatterer on the target is given by

$$H(\vec{r}_r, \vec{r}_b[n]) = \frac{e^{-jk||\vec{r}_r - \vec{r}_b[n]||}}{||\vec{r}_r - \vec{r}_b[n]||} + \Gamma(\theta_b)\frac{e^{-jk||\vec{r}_r - \vec{r}_{b'}[n]||}}{||\vec{r}_r - \vec{r}_{b'}[n]||}. \quad (5)$$

In the above expression, $\Gamma(\theta_b)$ is the Fresnel reflection coefficient computed for vertical polarization for an incident angle of θ_b. Some recent works [12, 46] describe computation of exact coefficients under specific UAV channel conditions.

3.2. Electromagnetic scattering center models

The motion of each of the road targets - car and pedestrian - is modeled using computer animation software based on the techniques described in [47–49]. In this work, we consider a mid-sized sedan that is animated by PyBullet, a physics simulation software as described in [18]. For a specified trajectory, the software describes realistic motions of the car involving accelerating from rest, reaching a steady speed and executing turns at video frame rates (30Hz/48Hz/60Hz). Then, we render the three-dimensional body of the car into multiple triangular facets and identify point scatterers at the centroids of each of these facets. Similar point scatterers along the wheel periphery to capture the dynamics of the wheel rotation. The chassis of the car and the spokes of the wheel are assumed to be made of perfect electric conductor with a reflection coefficient of 1. Each point scatterer is assumed to have a reflectivity, a_b, that is a function of the area (A_b) and length (d_b) of the corresponding facet and the angle of incidence, θ_b, from the radar as shown in

$$a_b = 2\sqrt{\pi}\frac{A_b \cos\theta_b[n]}{\lambda}\left(\frac{\sin\left(kd_b \sin\frac{\theta_b[n]}{2}\right)}{kd_b \sin\frac{\theta_b[n]}{2}}\right)^2. \quad (6)$$

Here k and λ are the propagation constant and wavelength of the radar respectively. In the case of the human, computer animation data describe the skeleton structure of the body and describe its motion at a video frame rate. We assume that each of the body is composed of an diectric ellipsoidal primitive whose reflectivity is again a function of the dimensions of the primitive and the angle of incidence as shown in

$$a_b[n] = \Gamma(\theta_b)\left(\frac{\frac{1}{4}R_b^4 H_b^2}{R_b^2 \sin^2\theta_b[n] + \frac{1}{4}H_b^2\cos^2\theta_b[n]}\right)^{\frac{1}{2}}. \quad (7)$$

The reflection coefficient shown in the above expression is computed from the Fresnel reflection coefficient for planar interfaces. The ellipsoid is assumed to be a homogeneous dielectric body of dielectric constant $3 - j3$ which corresponds to skin at millimeter wave frequencies. The computer animation data is interpolated from video frame rates to radar sampling frequencies. Then the electromagnetic scattering center model is

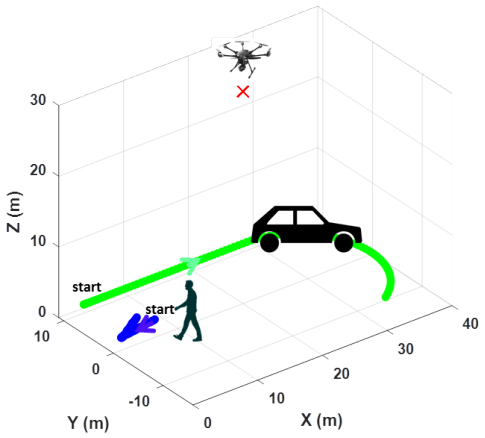

Fig. 2. Ten second long trajectory of car (green) and pedestrian (blue) below the UAV based radar mounted at (20,0,30)m.

3.3. Surface clutter model

The UAV-ground link discussed in the previous section modeled the effect of an infinite planar dielectric ground surface. We have further incorporated speckle noise in the radar range-Doppler ambiguity plots to model the statistical distribution of clutter scatterers and roughness in the surface. The clutter power is a function of the clutter cross section per unit area, denoted by σ^0. which is a function of the ground dielectric constant, the grazing angle ψ and the wetness of the surface. For a unit EIRP, the mean clutter noise power from a land surface at slant range r is given by

$$N_c(r, f_d) = \sigma^0\theta_{bw}\left(\frac{c\Delta\tau}{2}\right)\frac{\sec\psi}{(4\pi)^2 r^3}\left(1 + \frac{\Delta f_d}{f_d}\right)^n \quad (8)$$

where θ_{bw} and $\Delta\tau$ indicate the beamwidth and the pulse width of the transmitted radar signal [34]. The second term in the above expression shows the Doppler (f_d) based clutter arising due to wind or other propagation conditions. Here, Δf_d shows the ...which is a function of wind speed. The mean noise power is incorporated as complex speckle noise voltage in each cell of the the range-Doppler ambiguity plot. The magnitude of each cell is a Gaussian random variable of $\mathcal{N}(0, \sqrt{N_c/2})$ and the phase is a uniform random variable from $[0, 2\pi)$.

4. EXPERIMENTAL RESULTS

The radar, target and channel parameters that we simulated are presented in Table.1. We assume that a target is moving on a flat dielectric ground plane at $z = 0m$. A UAV mounted with a radar hovers at a fixed position, $\vec{r}_r : (20, 0, 30)$m, at a low altitude above the ground plane. We consider two types of targets - a car and a pedestrian - whose trajectories are shown in Fig.2. The center of gravity of the car begins from a position of $(3.3, 10.3, 1)$m and moves along a straight line and then turns to $(33.2, -11, 0.9)$m. The pedestrian walks along a straight line starting from $(8, 2, 1)$m and then turns around and walks away to $(6.7, 2.9, 1)$m. We assume that the propagation channel consists of only one target at a time. Therefore, the pedestrian and car motions are considered separately. The duration of the motion in each case is 10 seconds. The pedestrian motion is

Table 1. Simulation Model Parameters of Radar, Target and Ground Clutter

Parameters	Values
Equivalent isotropic radiated power (EIRP)	0dBW
Coherent processing interval (CPI)	8.2ms
Pulse repetition interval (PRI)	$2\mu s$
Bit rate ($F_s = 1/\Delta\tau$)	1.76GHz
Maximum unambiguous range	44m
Range resolution (Δr)	0.085m
Radar beamwidth (θ_{bw})	60°
Car size	$(4.5 \times 2 \times 0.56)$m
Pedestrian size	$(0.49 \times 0.6 \times 1.7)$m
Clutter cross-section area coefficient (σ^0)	$-15dB$
Doppler	

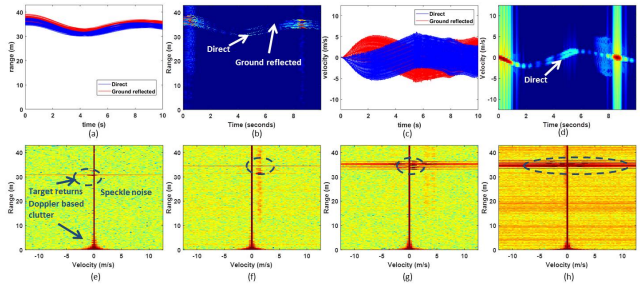

Fig. 3. Car signatures gathered by UAV based radar: (a) Ground truth and (b) radar based high range resolution profile including direct and surface reflected components. (c) Ground truth and (d) radar based Doppler-time spectrograms including direct and surface reflected components. (e)-(g) Range-Doppler ambiguity plots at 4, 5.7, 7.4 and 9s including target returns, ground clutter based speckle noise and Doppler based clutter.

described by computer animation data at a frame rate of 60Hz which is interpolated to the radar bit rate. The pedestrian model consists of 18 body parts that are connected together. We assume that in each scenario, the target always remains within the line of sight of the radar. Due to the low altitude of the radar mount, the target is always within maximum unambiguous range of the radar (44m). At these short ranges, the target may be regarded as an extended target with multiple point scatterers. The position of each of the point scatterers during each n^{th} sampling time instant is given by $\vec{r}_b[n], b = 1 : B$. The radar returns from the target interfere with ground based clutter and speckle noise. We assume that the equivalent isotropic radiated power (EIRP) from the radar transmitter is 0dBW. We present the radar signatures of the car from the UAV based radar in Fig.3. The range and Doppler variation of the multiple point scatterers on the body of the car are presented in Fig.3a and c. In both figures, we show the effects from the direct reflection (in blue) and the ground reflected components (in red). As expected, the range from the direct reflected components are shorter than the ground reflected components. The Doppler velocity components from the ground reflected components are opposite in sign to the direct components. Fig.3b and d show the range-time and Doppler-time signatures obtained from the ambiguity diagrams. For every CPI, the peaks across the range dimension are coherently summed to obtain the Doppler-time signatures. Likewise, the peaks across the Doppler dimension are coherently summed to obtain the range-time signatures. Both these

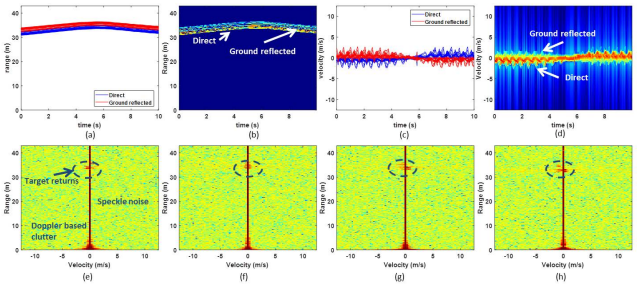

Fig. 4. Pedestrian signatures gathered by UAV based radar. (a) Ground truth and (b) radar based high range resolution profile including direct and surface reflected components. (c) Ground truth and (d) radar based Doppler-time spectrograms including direct and surface reflected components. (e)-(g) Range-Doppler ambiguity plots at 4, 5.7, 7.4 and 9s including target returns, ground clutter based speckle noise and Doppler based clutter.

figures are very close to the ground truth results discussed earlier. We observe that the ground reflected components are weaker than the direct components due to the reflection coefficient and the longer range. In these two figures, we have not considered the speckle noise arising from surface clutter or Doppler based clutter. They have however been considered for the remaining four range-Doppler ambiguity plots. The range-Doppler ambiguity plots for four different time instants (4,5,7,7,4 and 9s) are presented in Figs.3e-h. In all of these cases, we observe the target returns at range bins around 30m and Dopplers close to 0Hz. We observe strong static clutter at the DC bin. The Doppler based clutter falls off for higher frequencies. We also notice the background speckle noise in the images.

We repeat the simulations for the pedestrian and the results are presented in Fig.4. Again, we observe that the range-time (Fig.4b) and Doppler-time (Fig.4d) radar signatures closely map to the ground truth results presented in Fig.4a and c respectively. The range-extent of the pedestrian is much smaller than the span of the car. However, the micro-Doppler features from the motions of the arms and legs are more prominent in the Doppler-time signatures unlike the rigid body motion of the different parts of the car. Again the range-Doppler ambiguity plots show the target returns along with speckle noise from surface clutter and Doppler based clutter. Due to the slow speed of the pedestrian, there is greater overlap with the Doppler based clutter here. Also, the strength of the returns from the pedestrian are noticeably weaker than that of the car due to the smaller cross-section and the dielectric nature of the human bodies.

5. SUMMARY

We presented UAV-borne 802.11ad radar sensing of dynamic targets. Our pyBullet modeling allows for accounting for micro-Doppler signatures, surface clutter, and realistic electromagnetic scattering center models. In the future, similar techniques could be extended to a swarm-borne ground target sensing or UAV-to-UAV JRC [50]. Further, the effect of this system on communications performance may also be explored.

6. REFERENCES

[1] M. Mozaffari, W. Saad, M. Bennis, and M. Debbah, "Efficient deployment of multiple unmanned aerial vehicles for optimal wireless coverage," *IEEE Communications Letters*, vol. 20, no. 8, pp. 1647–1650, 2016.

[2] Y. Zeng, R. Zhang, and T. J. Lim, "Wireless communications with unmanned aerial vehicles: Opportunities and challenges," *IEEE Communications Magazine*, vol. 54, no. 5, pp. 36–42, May 2016.

[3] T. Tozer and D. Grace, "High-altitude platforms for wireless communications," *IET Electronics & communication engineering journal*, vol. 13, no. 3, pp. 127–137, 2001.

[4] N. R. Zema, E. Natalizio, and E. Yanmaz, "An unmanned aerial vehicle network for sport event filming with communication constraints," in *IEEE International Balkan Conference on Communications and Networking*, 2017.

[5] Y. Rong, R. Gutierrez, K. V. Mishra, and D. W. Bliss, "Noncontact vital sign detection with UAV-borne radars: An overview of recent advances," *IEEE Vehicular Technology Magazine*, vol. 16, no. 3, pp. 118–128, 2021.

[6] K. P. Valavanis and G. J. Vachtsevanos, *Handbook of unmanned aerial vehicles*. Springer, 2015, vol. 1.

[7] U. Challita, W. Saad, and C. Bettstetter, "Interference management for cellular-connected UAVs: A deep reinforcement learning approach," *IEEE Transactions on Wireless Communications*, vol. 18, no. 4, pp. 2125–2140, 2019.

[8] C. Wang, J. Wang, Y. Shen, and X. Zhang, "Autonomous navigation of UAVs in large-scale complex environments: A deep reinforcement learning approach," *IEEE Transactions on Vehicular Technology*, vol. 68, no. 3, pp. 2124–2136, 2019.

[9] X. Liu, Y. Liu, and Y. Chen, "Machine learning empowered trajectory and passive beamforming design in UAV-RIS wireless networks," *IEEE Journal on Selected Areas in Communications*, vol. 39, no. 7, pp. 2042–2055, 2021.

[10] M. Mozaffari, W. Saad, M. Bennis, and M. Debbah, "Communications and control for wireless drone-based antenna array," *IEEE Transactions on Communications*, vol. 67, no. 1, pp. 820–834, 2019.

[11] M. Alaee-Kerahroodi, K. V. Mishra, and B. S. MR, "Radar beampattern design for a drone swarm," in *Asilomar Conference on Signals, Systems, and Computers*, 2019, pp. 1416–1421.

[12] M. B. Ghorbel, D. Rodríguez-Duarte, H. Ghazzai, M. J. Hossain, and H. Menouar, "Joint position and travel path optimization for energy efficient wireless data gathering using unmanned aerial vehicles," *IEEE Transactions on Vehicular Technology*, vol. 68, no. 3, pp. 2165–2175, 2019.

[13] H. Lu, Y. Zeng, S. Jin, and R. Zhang, "Aerial intelligent reflecting surface: Joint placement and passive beamforming design with 3d beam flattening," *IEEE Transactions on Wireless Communications*, vol. 20, no. 7, pp. 4128–4143, 2021.

[14] Q. Wu, J. Xu, Y. Zeng, D. W. K. Ng, N. Al-Dhahir, R. Schober, and A. L. Swindlehurst, "A comprehensive overview on 5G-and-beyond networks with UAVs: From communications to sensing and intelligence," *IEEE Journal on Selected Areas in Communications*, 2021.

[15] L. Wu, K. V. Mishra, M. R. Bhavani Shankar, B. Ottersten *et al.*, "Resource allocation in heterogeneously-distributed joint radar-communications under asynchronous Bayesian tracking framework," *IEEE Journal on Selected Areas in Communications*, 2022, in press.

[16] K. V. Mishra, M. R. Bhavani Shankar, V. Koivunen, B. Ottersten, and S. A. Vorobyov, "Toward millimeter wave joint radar communications: A signal processing perspective," *IEEE Signal Processing Magazine*, vol. 36, no. 5, pp. 100–114, 2019.

[17] A. M. Elbir, K. V. Mishra, and S. Chatzinotas, "Terahertz-band joint ultra-massive MIMO radar-communications: Model-based and model-free hybrid beamforming," *IEEE Journal of Special Topics in Signal Processing*, vol. 15, no. 6, pp. 1468–1483, 2021.

[18] G. Duggal, S. Vishwakarma, K. V. Mishra, and S. S. Ram, "Doppler-resilient 802.11 ad-based ultrashort range automotive joint radar-communications system," *IEEE Transactions on Aerospace and Electronic Systems*, vol. 56, no. 5, pp. 4035–4048, 2020.

[19] M. Alaee-Kerahroodi, K. V. Mishra, M. R. B. Shankar, and B. Ottersten, "Discrete phase sequence design for coexistence of MIMO radar and MIMO communications," in *IEEE International Workshop on Signal Processing Advances in Wireless Communications*, 2019, pp. 1–5.

[20] S. H. Dokhanchi, M. R. Bhavani Shankar, K. V. Mishra, and B. Ottersten, "A mmWave automotive joint radar-communication system," *IEEE Transactions on Aerospace and Electronic Systems*, vol. 55, no. 3, pp. 1241–1260, 2019.

[21] G. Duggal, S. S. Ram, and K. V. Mishra, "Micro-Doppler and micro-range detection via Doppler-resilient 802.11ad-based vehicle-to-pedestrian radar," in *IEEE Radar Conference*, 2019, pp. 1–6.

[22] P. Kumari, J. Choi, N. González-Prelcic, and R. W. Heath, "IEEE 802.11ad-based radar: An approach to joint vehicular communication-radar system," *IEEE Transactions on Vehicular Technology*, vol. 67, no. 4, pp. 3012–3027, 2018.

[23] H. Ullah, M. Abu-Tair, S. McClean, P. Nixon, G. Parr, and C. Luo, "Connecting disjoint nodes through a UAV-based wireless network for bridging communication using IEEE 802.11 protocols," *EURASIP Journal on Wireless Communications and Networking*, vol. 2020, no. 1, pp. 1–20, 2020.

[24] D. Garcia, J. O. Lacruz, P. J. Mateo, and J. Widmer, "POLAR: Passive object localization with IEEE 802.11ad using phased antenna arrays," in *IEEE Conference on Computer Communications*, 2020, pp. 1838–1847.

[25] N. González-Prelcic, R. Méndez-Rial, and R. W. Heath Jr., "Radar aided beam alignment in MmWave V2I communications supporting antenna diversity," in *IEEE Information Theory and Applications Workshop*, 2016.

[26] I. Mavromatis, A. Tassi, R. J. Piechocki, and A. Nix, "Beam alignment for millimetre wave links with motion prediction of autonomous vehicles," in *IET Colloquium on Antennas, Propagation & RF Technology for Transport and Autonomous Platforms*, 2017, pp. 1–8.

[27] G. R. Muns, K. V. Mishra, C. B. Guerra, Y. C. Eldar, and K. R. Chowdhury, "Beam alignment and tracking for autonomous vehicular communication using IEEE 802.11ad-based radar," in *IEEE Infocom Workshops - Hot Topics in Social and Mobile Connected Smart Objects*, 2019, pp. 535–540.

[28] P. Kumari, N. González-Prelcic, and R. W. Heath Jr., "Investigating the IEEE 802.11ad standard for millimeter wave automotive radar," in *IEEE Vehicular Technology Conference - Spring*, 2015, pp. 1–5.

[29] M. J. E. Golay, "Complementary series," *IRE Transactions on Information Theory*, vol. 7, no. 2, pp. 82–87, 1961.

[30] K. V. Mishra and Y. C. Eldar, "Sub-Nyquist channel estimation over IEEE 802.11ad link," in *IEEE International Conference on Sampling Theory and Applications*, 2017, pp. 355–359.

[31] A. Pezeshki, A. R. Calderbank, W. Moran, and S. D. Howard, "Doppler resilient Golay complementary waveforms," *IEEE Transactions on Information Theory*, vol. 54, no. 9, pp. 4254–4266, 2008.

[32] G. Han and J. Choi, "Radar imaging based on IEEE 802.11ad waveform," in *IEEE Global Communications Conference*, 2020, pp. 1–6.

[33] J. R. Guerci, *Cognitive radar: The knowledge-aided fully adaptive approach*. Artech House, 2010.

[34] M. I. Skolnik, *Radar handbook*, 3rd ed. McGraw-Hill, 2008.

[35] K. D. Ward, S. Watts, and R. J. Tough, *Sea clutter: Scattering, the K distribution and radar performance*. IET, 2006, vol. 20.

[36] G. P. Kulemin, *Millimeter-wave radar targets and clutter*. Artech House, 2003.

[37] J. B. Billingsley, *Low-angle radar land clutter: Measurements and empirical models*. IET, 2002.

[38] Y. H. Mao, "MTI, MTD and adaptive clutter cancellation," in *Advanced Radar Techniques and Systems*, G. Galati, Ed. Peter Peregrinus, 1993, pp. 285–442.

[39] H. L. Van Trees, *Detection, estimation, and modulation theory*. John Wiley & Sons, 2004.

[40] J. E. Cilliers and J. C. Smit, "Pulse compression sidelobe reduction by minimization of l_p-norms," *IEEE Transactions on Aerospace and Electronic Systems*, vol. 43, no. 3, pp. 1238–1247, 2007.

[41] K. V. Mishra, V. Chandrasekar, C. Nguyen, and M. Vega, "The signal processor system for the NASA dual-frequency dual-polarized Doppler radar," in *IEEE International Geoscience and Remote Sensing Symposium*, 2012, pp. 4774–4777.

[42] M. T. Dabiri, M. Rezaee, I. S. Ansari, and V. Yazdanian, "Channel modeling for UAV-based optical wireless links with nonzero boresight pointing errors," *IEEE Transactions on Vehicular Technology*, vol. 69, no. 12, pp. 14 238–14 246, 2020.

[43] M. T. Dabiri, H. Safi, S. Parsaeefard, and W. Saad, "Analytical channel models for millimeter wave UAV networks under hovering fluctuations," *IEEE Transactions on Wireless Communications*, vol. 19, no. 4, pp. 2868–2883, 2020.

[44] D. W. Matolak and R. Sun, "Unmanned aircraft systems: Air-ground channel characterization for future applications," *IEEE Vehicular Technology Magazine*, vol. 10, no. 2, pp. 79–85, 2015.

[45] S. S. Ram, R. Bhalla, and H. Ling, "Simulation of human radar signatures in the presence of ground," in *IEEE Antennas and Propagation Society International Symposium*, 2009, pp. 1–4.

[46] A. Al-Hourani, S. Kandeepan, and S. Lardner, "Optimal LAP altitude for maximum coverage," *IEEE Wireless Communications Letters*, vol. 3, no. 6, pp. 569–572, 2014.

[47] S. S. Ram and H. Ling, "Simulation of human microDopplers using computer animation data," in *IEEE Radar Conference*, 2008, pp. 1–6.

[48] S. S. Ram, C. Christianson, and H. Ling, "Simulation of high range-resolution profiles of humans behind walls," in *IEEE Radar Conference*, 2009, pp. 1–4.

[49] S. S. Ram, C. Christianson, Y. Kim, and H. Ling, "Simulation and analysis of human micro-Dopplers in through-wall environments," *IEEE Transactions on Geoscience and Remote Sensing*, vol. 48, no. 4, pp. 2015–2023, 2010.

[50] M. Polese, L. Bertizzolo, L. Bonati, A. Gosain, and T. Melodia, "An experimental mmWave channel model for UAV-to-UAV communications," in *ACM Workshop on Millimeter-Wave Networks and Sensing Systems*, 2020, pp. 1–6.